JOURNAL OF THERMOPHYSICS AND HEAT TRANSFER
Vol. 25, No. 2, April–June 2011

Exact Solution of Radiative Transfer Equation for Three-Dimensional Rectangular, Linearly Scattering Medium

Zekeriya Altaç* and Mesut Tekkalmaz†
Eskişehir Osmangazi University, 26480 Eskişehir, Turkey

DOI: 10.2514/1.50910

Three-dimensional radiative integral transfer equations for a cubic absorbing, emitting, and anisotropically scattering homogeneous medium are solved. To remove existing singularities of the radiative integral transfer equations, the surface and volume integrals arising from the application of the subtraction of the singularity technique are analytically treated to ensure highly accurate solutions and to reduce the computational time. The resulting system of linear equations from the integral equations of the incident energy and the net partial heat fluxes are solved iteratively. Three benchmark problems for a cold participating medium, subjected to externally diffuse radiation loads in various combinations, are considered. The solutions for the incident energy and the net partial radiative heat fluxes are given in tabular and/or graphical form for scattering albedos of $\omega_0 = 0.01$, 0.5, and 1.

Nomenclature

$\bar{a}$	=	coefficient of linear anisotropy
a_1, a_2	=	source patch intervals in x direction, as shown in Fig. 1
b_1, b_2	=	source patch intervals in y direction, as shown in Fig. 1
d	=	optical distance between (x, y, z) and $(x', y', 0)$
dA_G, dA_x, dA_y, dA_z, dA_{nm}	=	dimensionless area elements defined in Table 1
E_2	=	second-order exponential integral function
F_G, F_x, F_y, F_z, F_{nm}	=	integrals defined by Eqs. (12–14)
f_G, f_x, f_y, f_z	=	integrals defined by Eqs. (7–9)
G	=	dimensionless incident energy, $g/\sigma T_0^4$
g	=	incident energy, $\mathrm{W/m^2}$
I	=	dimensionless radiation intensity, $i/\sigma T_0^4$
i	=	radiation intensity, $\mathrm{W/m^2 \cdot sr}$
I_D	=	dimensionless diffuse patch intensity
m	=	optical dimensions x, y, or z
N	=	number of grid points
$\mathbf{n}$	=	unit vector normal to surface
n	=	optical dimensions x, y, or z
$\mathbf{Q}$	=	radiative heat flux, $\mathrm{W/m^2}$
$\mathbf{q}$	=	dimensionless radiative heat flux, $\mathbf{Q}/\sigma T_0^4$
q_x, q_y, q_z	=	dimensionless radiative heat flux components
$\mathbf{r}$	=	position vector (x, y, z)
S	=	dimensionless isotropic medium source function defined by Eq. (3), $s/\sigma T_0^4$
s	=	isotropic medium source function, $\mathrm{W/m^2}$
S_a	=	dimensionless anisotropic medium source function defined by Eq. (4), $s_a/\sigma T_0^4$
s_a	=	anisotropic medium source function, $\mathrm{W/m^2}$
T	=	temperature, K
V	=	domain volume, $\mathrm{m^3}$
V_G, V_x, V_y, V_z, V_{nm}	=	integrals defined by Eqs. (16), (17), and (19)
V_i	=	pyramidal domains, as labeled 1, 2, 3, 4, 5, or 6 in Fig. 2b.
w_{ni}	=	Newton–Cotes weights for x, y, or z
X, Y, Z	=	coordinate variables, m
x, y, z	=	optical coordinates, $\beta(X, Y, Z)$
β	=	extinction coefficient, $1/\mathrm{m}$
Γ	=	surface of enclosure
Δu	=	step size (x, y, or z)
θ	=	zenith angle, rad
θ_{ia}, θ_{ib}	=	zenith angles for ith pyramid, as shown in Fig. 2a, rad
κ	=	absorption coefficient, $1/\mathrm{m}$
ξ_i	=	projection angles shown in Fig. 3 (1, 2, 3, and 4), rad
ρ	=	optical distance from (x', y', z') to (x, y, z)
ρ_i	=	optical distances from (x', y', z') to enclosing 1, 2, 3, 4, 5, and 6 surfaces, Fig. 2
σ	=	Stefan–Boltzmann constant, $\mathrm{W/m^2\,K^4}$
σ_s	=	scattering coefficient, $1/\mathrm{m}$
φ	=	azimuthal angle, rad
ϕ_i	=	projection angles, as shown in Fig. 3 (1, 2, 3, and 4), rad
$\mathbf{\Omega}_0$	=	scattering direction
ω_0	=	single scattering albedo, σ_s/β

Subscripts

G	=	incident energy
i, j, k	=	integration quadrature/weights indices
ijk	=	shorthand notation for f_{ijk}
n, m	=	component indices (x, y, or z for both)
x, y, z	=	direction indices
0	=	reference or surface

Superscript

$'$	=	dummy integration variable

Received 25 May 2010; revision received 7 December 2010; accepted for publication 12 December 2010.

*Mechanical Engineering Department, School of Engineering and Architecture, 26480 Batı Meşelik; zaltac@ogu.edu.tr.

†Metallurgical and Materials Engineering Department, School of Engineering and Architecture, 26480 Batı Meşelik; tmesut@ogu.edu.tr.

I. Introduction

RADIATIVE heat transfer in participating media is an important consideration in designing combustors, nuclear reactors, many industrial processes, and solar energy systems. In recent years, much attention has been paid to the numerical solution of radiative heat

transfer in multidimensional participating media, including radiation with anisotropic scattering.

Because of the complexity of this problem, early studies involving anisotropic scattering of thermal radiation were considered in one dimension [1–5]. Stephens [6] presented a doubling formulation to be applied to optically thick two-dimensional anisotropically scattering media and demonstrated the technique for some isotropic scattering cases as well. Kim and Lee [7] investigated radiative energy transfer in two-dimensional rectangular enclosures, with gray, absorbing, emitting, and anisotropically scattering media, using the discrete ordinates method (DOM). A complete Mie-scattering phase function was also incorporated into the numerical solution. Tan [8] presented the mathematical formulation and related numerical method for general multidimensional radiative transfer in absorbing, emitting, and anisotropically scattering media. Thynell [9] formulated the radiative integral transfer equations (RITEs) for absorbing, emitting, and linear-anisotropically scattering two-dimensional cylindrical media bounded by emitting and diffusely reflecting walls. Two-dimensional exact integral equations for a cylindrical medium that scatters anisotropically were derived and numerically solved for various boundary conditions by Crosbie and Dougherty [10]. Altaç [11] solved the radiative transfer equation (RTE) for absorbing, emitting, and linearly anisotropically scattering inhomogeneous one-dimensional cylindrical media using the RITEs and subtraction of singularity technique. Altaç and Tekkalmaz [12] solved two-dimensional RITEs for a linearly anisotropic homogeneous rectangular medium using the same technique. Crosbie and Lee [13] derived the integral equation for the source function in a three-dimensional rectangular medium, which scatters anisotropically for spatially varying incident radiation. In the study, they used a double Fourier transform to reduce the problem to a one-dimensional integral equation for the source function.

Three-dimensional P_3 results were published by Mengüç and Viskanta [14]. A finite element solution for simulation of radiative heat transfer in absorbing, emitting, and anisotropically scattering media was reported by An et al. [15]. Boulet et al. [16] investigated the ability of the finite volume method (FVM) and the DOM to model radiative heat transfer in acute forward anisotropically scattering media. Jiang [17] presented a two-step procedure for the computation of radiative heat transfer with anisotropic scattering and reflection. Three-dimensional radiative transfer in an anisotropically scattering medium exposed to spatially varying, collimated radiation was studied by Mueller and Crosbie [18]. They used a generalized reflection function for a semi-infinite medium with a general scattering phase function, and an integral transform was adapted to reduce the three-dimensional transport equation to a one-dimensional form. A three-dimensional control volume finite element method for the treatment of the RTE applied to emitting, absorbing, and scattering media was developed by Grissa et al. [19]. Two numerical models for solving thermal radiative transport in irregularly shaped axisymmetric geometry containing homogeneous, anisotropically scattering media were presented by Nunes et al. [20].

The integral form of the three-dimensional RTE for an absorbing, emitting, and linear-anisotropically scattering medium with space-dependent properties was formulated by Zhang and Sutton [21]. The integral transfer equations in a two-dimensional axisymmetric and inhomogeneous medium subjected to externally incident radiation or bounded by emitting and diffusely reflecting walls were considered. The RTE was solved by Trivic and Amon [22] using the FVM and Mie scattering. A new angular discretization scheme for the FVM in three-dimensional radiative heat transfer was presented by Kim and Huh [23]. The method was applied to absorbing, emitting, and anisotropically scattering media with variable optical thickness in a rectangular enclosure.

Integrating over the solid angle, RITEs represent an exact formulation of the RTE. The advantage of using RITEs is that one deals with spatial variables only. On the other hand, the main drawback of RITEs is, for multidimensional and/or complex geometries, the radiative transfer kernels that appear in RITEs must be analytically derived from scratch. The numerical solution of RITEs requires analytical and/or numerical treatments for the singularities of the transfer kernels. On the other hand, solution of dense linear systems of equations, arising from the numerical solution of the integral equations, leads to excessive computational time. Exact or highly accurate numerical solutions of RITEs could serve as benchmark solutions for the development of new numerical methods and/or techniques.

With daily developments in computer technology, three-dimensional studies are becoming more and more attractive and feasible. Methods and/or techniques of higher accuracy with less computational time are sought by engineers and scientists in this field. When applying new methods or techniques to the RTE, it is important to know if the solutions are free of ray effects. Therefore, highly accurate benchmark solutions derived from the exact RITEs are extremely valuable in order to assess the accuracy and validity of new methods, approximations, or techniques proposed. The aim of this study is to provide benchmark solutions in tabular (four-significant-figure accurate) and/or graphical forms for three-dimensional rectangular absorbing and linearly anisotropically scattering homogeneous media.

II. Radiative Integral Transfer Equations

Radiative integral transfer equations for a three-dimensional absorbing, emitting, homogeneous with linear-anisotropically scattering medium are given by [11] for the incident energy:

$$G(\mathbf{r}) = \int_\Gamma I_0(\mathbf{r}_0, \mathbf{\Omega}_0) \frac{(\mathbf{r}_0 - \mathbf{r}) \cdot \mathbf{n} e^{-|\mathbf{r}_0 - \mathbf{r}|} \, \mathrm{d}\Gamma}{4\pi |\mathbf{r}_0 - \mathbf{r}|^3} + \int_V S_a(\mathbf{r}') \frac{e^{-|\mathbf{r} - \mathbf{r}'|} \, \mathrm{d}V'}{4\pi |\mathbf{r} - \mathbf{r}'|^2} \tag{1}$$

and for the net radiative heat flux:

$$\mathbf{q}(\mathbf{r}) = \int_\Gamma I_0(\mathbf{r}_0, \mathbf{\Omega}_0) \frac{(\mathbf{r} - \mathbf{r}_0)(\mathbf{r}_0 - \mathbf{r}) \cdot \mathbf{n} e^{-|\mathbf{r}_0 - \mathbf{r}|} \, \mathrm{d}\Gamma}{4\pi |\mathbf{r}_0 - \mathbf{r}|^4} + \int_V S_a(\mathbf{r}') \frac{(\mathbf{r} - \mathbf{r}') e^{-|\mathbf{r} - \mathbf{r}'|} \, \mathrm{d}V'}{4\pi |\mathbf{r} - \mathbf{r}'|^3} \tag{2}$$

where $\mathbf{r}$ is the optical coordinate; I_0 is the dimensionless radiation intensity of the surface at $\mathbf{r}_0$ in the $\mathbf{\Omega}_0 = (\mathbf{r}_0 - \mathbf{r})/|\mathbf{r}_0 - \mathbf{r}|$ direction; $\mathbf{n}$ is the unit vector normal to the surface Γ; $\mathrm{d}V'$ is the volume element; and $S(\mathbf{r})$ and $S_a(\mathbf{r})$ are, respectively, the dimensionless isotropic and anisotropic cold medium source functions defined as

$$S(\mathbf{r}) = \omega_0 G(\mathbf{r}) \tag{3}$$

$$S_a(\mathbf{r}') = \omega_0 G(\mathbf{r}) + \bar{a}\omega_0 \frac{(\mathbf{r} - \mathbf{r}')}{|\mathbf{r} - \mathbf{r}'|} \cdot \mathbf{q}(\mathbf{r}') \tag{4}$$

The RITE for a three-dimensional rectangular participating, anisotropically scattering, cold medium with a diffuse constant incident intensity, $I_0(\mathbf{r}_0, \mathbf{\Omega}_0) = I_D$, yields for the dimensionless incident energy

$$G(\mathbf{r}) = f_G(\mathbf{r}) + \int_V S(\mathbf{r}') \frac{e^{-|\mathbf{r} - \mathbf{r}'|} \, \mathrm{d}V'}{4\pi |\mathbf{r} - \mathbf{r}'|^2} + \bar{a}\omega_0 \times \sum_{m=x,y,z} \int_V (m - m') q_m(\mathbf{r}') \frac{e^{-|\mathbf{r} - \mathbf{r}'|} \, \mathrm{d}V'}{4\pi |\mathbf{r} - \mathbf{r}'|^3} \tag{5}$$

and for the dimensionless net radiative heat flux components

$$q_n(\mathbf{r}) = f_n(\mathbf{r}) + \int_V S(\mathbf{r}')(n - n') \frac{e^{-|\mathbf{r} - \mathbf{r}'|} \, \mathrm{d}V'}{4\pi |\mathbf{r} - \mathbf{r}'|^3} + \bar{a}\omega_0 \times \sum_{m=x,y,z} \int_V (n - n')(m - m') q_m(\mathbf{r}') \frac{e^{-|\mathbf{r} - \mathbf{r}'|} \, \mathrm{d}V'}{4\pi |\mathbf{r} - \mathbf{r}'|^4} \tag{6}$$

where $n = x, y$, and z, $\mathbf{r} = (x, y, z)$ and $\mathbf{r}' = (x', y', z')$ are the optical coordinates, and the optical distance is defined as

$$|\mathbf{r}-\mathbf{r}'| = \sqrt{(x-x')^2+(y-y')^2+(z-z')^2}$$

A rectangular patch at the bottom of an enclosure ($-a_1 \le x \le a_2$, $-b_1 \le y \le b_2$), which is subjected to external constant diffuse incident radiation (Fig. 1) is considered. Substituting $\mathbf{r}_0 = x'\mathbf{i} + y'\mathbf{j}$, $\mathbf{r} = x\mathbf{i} + y\mathbf{j} + z\mathbf{k}$, and $\mathbf{n} = \mathbf{k}$ into the surface integrals of Eqs. (5) and (6), one obtains the direct radiation incidence terms as

$$f_G(\mathbf{r}) = zI_D \int_{x'=-a_1}^{a_2}\int_{y'=-b_1}^{b_2} \frac{e^{-d}}{4\pi d^3}\,dx'\,dy' \tag{7}$$

$$f_n(\mathbf{r}) = zI_D \int_{x'=-a_1}^{a_2}\int_{y'=-b_1}^{b_2} \frac{e^{-d}}{4\pi d^4}(n-n')\,dx'\,dy', \quad \text{for } n = x, y \tag{8}$$

$$f_z(\mathbf{r}) = z^2 I_D \int_{x'=-a_1}^{a_2}\int_{y'=-b_1}^{b_2} \frac{e^{-d}}{4\pi d^4}\,dx'\,dy' \tag{9}$$

where $d = \sqrt{(x-x')^2+(y-y')^2+z^2}$. Singularities of Eqs. (7–9) are treated basically in the same manner as described in [24].

III. Problem Statement and Numerical Solution Technique

The system geometry of the enclosure is given in Fig. 1. The walls of the enclosure are assumed to be black. A rectangular patch at the bottom wall is subject to externally incident constant ($I_D = 1$) diffuse radiation. The numerical solution technique used to solve the RITEs is "subtraction of singularity," which is described for a three-dimensional medium in detail in [24]. In this paper, the technique is basically extended to linearly anisotropically scattering three-dimensional rectangular media. The rectangular domain V, bounded by $-x_0 \le x \le x_0$, $-y_0 \le y \le y_0$, and $0 \le z \le z_0$, is divided into equally spaced $N_x - 1$, $N_y - 1$, and $N_z - 1$ intervals, respectively. Five-point (or four interval) closed-type Newton–Cotes (Boole's rule) composite quadratures and weights [25] [(x_i, w_{xi}) for $i = 1, \ldots, N_x$, (y_i, w_{yi}) for $i = 1, \ldots, N_y$, and (z_i, w_{zi}) for $i = 1, \ldots, N_z$] are generated for the numerical integration. These quadrature sets have sixth-order approximation errors; that is, $\mathcal{O}(\Delta u^6)$ where Δu is the step size, with u being either x, y, or z. The composite numerical integration rule is also employed; that is, the integration over an interval is divided into smaller subintervals referred to as panels, and Boole's rule is applied on each panel. In Eqs. (5) and (6), the triple integrals are then replaced by their numerical integration sums yielding a triple sum. However, the terms $|\mathbf{r}-\mathbf{r}'|^2$, $|\mathbf{r}-\mathbf{r}'|^3$, and $|\mathbf{r}-\mathbf{r}'|^4$, which are the cause of the singularity, will yield erroneous solutions when $\mathbf{r}' \to \mathbf{r}$ if this singularity is not properly treated. For this reason, using Eq. (3), we add and subtract $S(\mathbf{r})e^{-|\mathbf{r}-\mathbf{r}'|}/|\mathbf{r}-\mathbf{r}'|^2$ and $q_n(\mathbf{r})e^{-|\mathbf{r}-\mathbf{r}'|}/|\mathbf{r}-\mathbf{r}'|^3$ terms inside the triple integrals of Eq. (5) as follows:

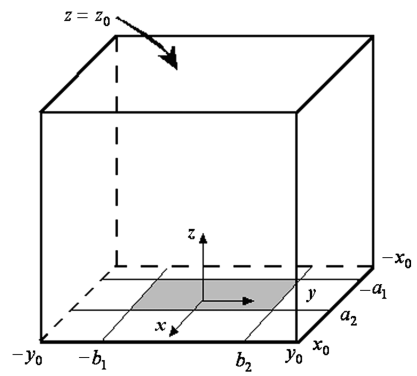

Fig. 1 Geometry, coordinate system, and boundary loading.

$$G(\mathbf{r}) = f_G(\mathbf{r}) + \omega_0 G(\mathbf{r})F_G(\mathbf{r}) + \bar{a}\omega_0\{q_x(\mathbf{r})F_x(\mathbf{r}) + q_y(\mathbf{r})F_y(\mathbf{r}) + q_z(\mathbf{r})F_z(\mathbf{r})\} + \omega_0\int_V [G(\mathbf{r}')-G(\mathbf{r})]\frac{e^{-|\mathbf{r}-\mathbf{r}'|}\,dV'}{4\pi|\mathbf{r}-\mathbf{r}'|^2} + \bar{a}\omega_0 \sum_{m=x,y,z}\int_V [q_m(\mathbf{r}')-q_m(\mathbf{r})](m-m')\frac{e^{-|\mathbf{r}-\mathbf{r}'|}\,dV'}{4\pi|\mathbf{r}-\mathbf{r}'|^3} \tag{10}$$

and a similar procedure is employed for Eq. (6) to give

$$q_n(\mathbf{r}) = f_n(\mathbf{r}) + \omega_0 G(\mathbf{r})F_n(\mathbf{r}) + \bar{a}\omega_0\{q_x(\mathbf{r})F_{nx}(\mathbf{r}) + q_y(\mathbf{r})F_{ny}(\mathbf{r}) + q_z(\mathbf{r})F_{nz}(\mathbf{r})\} + \omega_0\int_V [G(\mathbf{r}')-G(\mathbf{r})](n-n')\frac{e^{-|\mathbf{r}-\mathbf{r}'|}\,dV'}{4\pi|\mathbf{r}-\mathbf{r}'|^3} + \bar{a}\omega_0 \sum_{m=x,y,z}\int_V [q_m(\mathbf{r}')-q_m(\mathbf{r})](m-m')(n-n')\frac{e^{-|\mathbf{r}-\mathbf{r}'|}\,dV'}{4\pi|\mathbf{r}-\mathbf{r}'|^4}, \quad n = x, y, z \tag{11}$$

where

$$F_G(\mathbf{r}) = \int_V \frac{e^{-|\mathbf{r}-\mathbf{r}'|}}{4\pi|\mathbf{r}-\mathbf{r}'|^2}\,dV' \tag{12}$$

$$F_n(\mathbf{r}) = \int_V \frac{e^{-|\mathbf{r}-\mathbf{r}'|}}{4\pi|\mathbf{r}-\mathbf{r}'|^3}(n-n')\,dV' \tag{13}$$

$$F_{nm}(\mathbf{r}) = \int_V \frac{e^{-|\mathbf{r}-\mathbf{r}'|}}{4\pi|\mathbf{r}-\mathbf{r}'|^4}(m-m')(n-n')\,dV' \quad \text{for } n = m = x, y, z \tag{14}$$

Now, the terms in the square brackets of Eqs. (10) and (11) yield zero for $\mathbf{r}' = \mathbf{r}$, which properly eliminates the singularities due to the terms $1/|\mathbf{r}-\mathbf{r}'|^2$, $(n-n')/|\mathbf{r}-\mathbf{r}'|^3$, and $(n-n')(m-m')/|\mathbf{r}-\mathbf{r}'|^4$. However, in their present forms, Eqs. (12–14), which account for $\mathbf{r}' = \mathbf{r}$ cases, are still singular, and they require analytical treatments that are detailed in [24].

Next, replacing the integrals with their quadrature sums, using the shorthand notation for each quantity as $f(x_i, y_j, z_k) = f_{ijk}$, and rearranging Eq. (10) yields

$$G_{ijk} = f_{G,ijk} + \omega_0 G_{ijk}(F_G - V_G)_{ijk} + \omega_0\bar{a}\{q_x(F_x - V_x) + q_y(F_y - V_y) + q_z(F_z - V_z)\}_{ijk} + \omega_0 \sum_{\substack{i',j',k'=1 \\ i',j',k' \ne i,j,k}}^{N_x,N_y,N_z} w_{xi'}w_{yj'}w_{zk'}\frac{\exp(-|\mathbf{r}_{ijk}-\mathbf{r}_{i'j'k'}|)}{4\pi|\mathbf{r}_{ijk}-\mathbf{r}_{i'j'k'}|^2}G_{i'j'k'} + \omega_0\bar{a}\sum_{\substack{i',j',k'=1 \\ i',j',k' \ne i,j,k}}^{N_x,N_y,N_z} w_{xi'}w_{yj'}w_{zk'} \times \sum_{n=x,y,z}(n_i - n'_{i'})\frac{\exp(-|\mathbf{r}_{ijk}-\mathbf{r}_{i'j'k'}|)}{4\pi|\mathbf{r}_{ijk}-\mathbf{r}_{i'j'k'}|^3}q_{n,i'j'k'} \tag{15}$$

where

$$V_{G,ijk} = \sum_{\substack{i',j',k'=1 \\ i',j',k' \ne i,j,k}}^{N_x,N_y,N_z} w_{xi'}w_{yj'}w_{zk'}\frac{\exp(-|\mathbf{r}_{ijk}-\mathbf{r}_{i'j'k'}|)}{4\pi|\mathbf{r}_{ijk}-\mathbf{r}_{i'j'k'}|^2} \tag{16}$$

$$V_{n,ijk} = \sum_{\substack{i',j',k'=1 \\ i',j',k' \ne i,j,k}}^{N_x,N_y,N_z} w_{xi'}w_{yj'}w_{zk'}(n_i - n'_{i'})\frac{\exp(-|\mathbf{r}_{ijk}-\mathbf{r}_{i'j'k'}|)}{4\pi|\mathbf{r}_{ijk}-\mathbf{r}_{i'j'k'}|^3} \tag{17}$$

Similarly, using Eq. (11), the net radiative heat flux components are treated the same way to yield

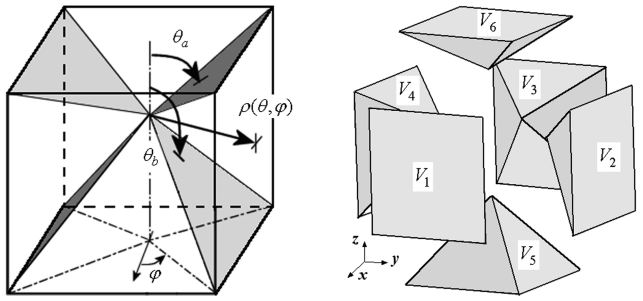

a) b)

Fig. 2 Spherical coordinate integration: a) schematic and b) enumerated pyramid volumes.

$$
\begin{aligned}
q_{n,ijk} &= f_{n,ijk} + \omega_0 G_{ijk}(F_n - V_n)_{ijk} + \omega_0 \bar{a}\{q_x(F_{nx} - V_{nx}) \\
&\quad + q_y(F_{ny} - V_{ny}) + q_z(F_{nz} - V_{nz})\}_{ijk} \\
&\quad + \omega_0 \sum_{\substack{i',j',k'=1 \\ i',j',k' \neq i,j,k}}^{N_x,N_y,N_z} w_{xi'} w_{yj'} w_{zk'} (n_i - n'_{i'}) \frac{\exp(-|\mathbf{r}_{ijk} - \mathbf{r}_{i'j'k'}|)}{4\pi |\mathbf{r}_{ijk} - \mathbf{r}_{i'j'k'}|^3} G_{i'j'k'} \\
&\quad + \omega_0 \bar{a} \sum_{\substack{i',j',k'=1 \\ i',j',k' \neq i,j,k}}^{N_x,N_y,N_z} w_{xi'} w_{yj'} w_{zk'} (n_i - n'_{i'}) \sum_{m=x,y,z} (m_i - m'_{i'}) \\
&\quad \times \frac{\exp(-|\mathbf{r}_{ijk} - \mathbf{r}_{i'j'k'}|)}{4\pi |\mathbf{r}_{ijk} - \mathbf{r}_{i'j'k'}|^4} q_{m,i'j'k'}, \qquad n = x, y, z
\end{aligned} \tag{18}
$$

where

$$
\begin{aligned}
V_{nm,ijk} &= \sum_{\substack{i',j',k'=1 \\ i',j',k' \neq i,j,k}}^{N_x,N_y,N_z} w_{xi'} w_{yj'} w_{zk'} (m_i - m'_{i'})(n_i - n'_{i'}) \\
&\quad \times \frac{\exp(-|\mathbf{r}_{ijk} - \mathbf{r}_{i'j'k'}|)}{4\pi |\mathbf{r}_{ijk} - \mathbf{r}_{i'j'k'}|^4}
\end{aligned} \tag{19}
$$

Equations (15) and (18) constitute a system of linear equations for the incident energy and the net radiative heat flux components, which is solved iteratively. The evaluation of the volume integrals given by Eqs. (12–14) are partially carried out analytically. Defining the spherical coordinate system as $x' - x = \rho \sin\theta \cos\varphi$, $y' - y = \rho \sin\theta \sin\varphi$, and $z' - z = \rho \cos\theta$ yields $|\mathbf{r} - \mathbf{r}'| = \rho$ and

$$
\mathrm{d}V' = \mathrm{d}x' \, \mathrm{d}y' \, \mathrm{d}z' = \rho^2 \sin\theta \, \mathrm{d}\rho \, \mathrm{d}\theta \, \mathrm{d}\varphi
$$

(Fig. 2a). For an interior node, the medium is divided into six rectangular pyramids (Fig. 2b). To save space, the procedure used for the analytical integrations is illustrated for an interior grid node only. The integration over the distance ρ yields

$$
\int_0^{\rho_i} e^{-\rho} \, \mathrm{d}\rho = 1 - e^{-\rho_i}
$$

where ρ_i are the distances to the six enclosing surfaces, which are defined as

$$
\begin{aligned}
\rho_1 &= (x_0 - x)\csc\theta \sec\varphi, & \rho_2 &= (y_0 - y)\csc\theta \sec\varphi \\
\rho_3 &= (x_0 + x)\csc\theta \sec\varphi & \rho_4 &= (y_0 + y)\csc\theta \sec\varphi \\
\rho_5 &= -z \sec\theta, & \rho_6 &= (z_0 - z)\sec\theta
\end{aligned} \tag{20}
$$

To identify the integration domain of each pyramid V_k, $k = 1, \ldots, 6$, in the spherical coordinate system, we define the following zenith angles:

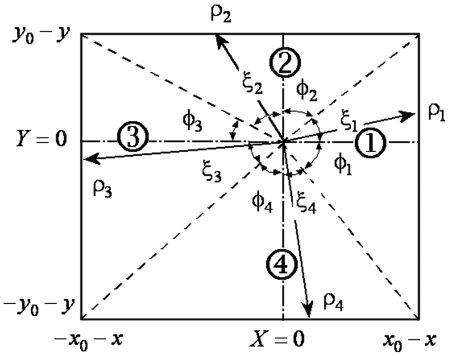

Fig. 3 Projection of pyramid volumes on the *xy* plane.

$$
\begin{aligned}
\theta_{1a} &= \tan^{-1}\left[\frac{x_0 - x}{(z_0 - z)\cos\varphi}\right], & \theta_{1b} &= \pi - \tan^{-1}\left[\frac{x_0 - x}{z\cos\varphi}\right] \\
\theta_{2a} &= \tan^{-1}\left[\frac{y_0 - y}{(z_0 - z)\cos\varphi}\right], & \theta_{2b} &= \pi - \tan^{-1}\left[\frac{y_0 - y}{z\cos\varphi}\right] \\
\theta_{3a} &= \tan^{-1}\left[\frac{x_0 + x}{(z_0 - z)\cos\varphi}\right], & \theta_{3b} &= \pi - \tan^{-1}\left[\frac{x_0 + x}{z\cos\varphi}\right] \\
\theta_{4a} &= \tan^{-1}\left[\frac{y_0 + y}{(z_0 - z)\cos\varphi}\right], & \theta_{4b} &= \pi - \tan^{-1}\left[\frac{y_0 + y}{z\cos\varphi}\right]
\end{aligned} \tag{21}
$$

On the other hand, the azimuthal variation of each domain V_k is determined from the projection of the pyramids (Fig. 2b) on the xy plane. The following angles can be easily deduced with the aid of Fig. 3:

$$
\begin{aligned}
\xi_1 &= \tan^{-1}\left(\frac{y_0 - y}{x_0 - x}\right), & \xi_2 &= \tan^{-1}\left(\frac{x_0 + x}{y_0 - y}\right) \\
\xi_3 &= \tan^{-1}\left(\frac{y_0 + y}{x_0 + x}\right), & \xi_4 &= \tan^{-1}\left(\frac{x_0 - x}{y_0 + y}\right) \\
\phi_1 &= \tan^{-1}\left(\frac{y_0 + y}{x_0 - x}\right), & \phi_2 &= \tan^{-1}\left(\frac{x_0 - x}{y_0 - y}\right) \\
\phi_3 &= \tan^{-1}\left(\frac{y_0 - y}{x_0 + x}\right), & \phi_4 &= \tan^{-1}\left(\frac{x_0 + x}{y_0 + y}\right)
\end{aligned} \tag{22}
$$

Taking into account the symmetry and trigonometric identities, the area elements are given in Table 1. Using Eqs. (20–22) and the area elements from Table 1, Eq. (12) yields the following expression:

$$
\begin{aligned}
F_G(\mathbf{r}) &= \sum_{k=1}^{6} \int_{V_k} e^{-\rho} \, \mathrm{d}\rho \, \mathrm{d}A_G = \sum_{i=1}^{4} \int_{\varphi=-\phi_i}^{\xi_i} \left\{ \int_{\theta=0}^{\theta_{ia}} (1 - e^{-\rho_6}) \, \mathrm{d}A_G \right. \\
&\quad \left. + \int_{\theta=\theta_{ia}}^{\theta_{ib}} (1 - e^{-\rho_i}) \, \mathrm{d}A_G + \int_{\theta=\theta_{ib}}^{\pi} (1 - e^{-\rho_5}) \, \mathrm{d}A_G \right\}
\end{aligned} \tag{23}
$$

Table 1 Definition of the area elements for each integral

n	m	Area element, $\mathrm{d}A_n$ or $\mathrm{d}A_{nm}$
G		$\sin\theta \, \mathrm{d}\theta \, \mathrm{d}\varphi$
x		$-\sin^2\theta \cos(\varphi + i\pi/2) \, \mathrm{d}\theta \, \mathrm{d}\varphi$
y		$-\sin^2\theta \sin(\varphi + i\pi/2) \, \mathrm{d}\theta \, \mathrm{d}\varphi$
z		$-\sin\theta \cos\theta \, \mathrm{d}\theta \, \mathrm{d}\varphi$
x	x	$\sin^3\theta \cos^2(\varphi + i\pi/2) \, \mathrm{d}\theta \, \mathrm{d}\varphi$
x	y	$-\sin^2\theta \sin(\varphi + i\pi/2) \cos(\varphi + i\pi/2) \, \mathrm{d}\theta \, \mathrm{d}\varphi$
x	z	$\sin^2\theta \cos\theta \cos(\varphi + i\pi/2) \, \mathrm{d}\theta \, \mathrm{d}\varphi$
y	y	$\sin^3\theta \sin^2(\varphi + i\pi/2) \, \mathrm{d}\theta \, \mathrm{d}\varphi$
y	z	$-\sin^2\theta \cos\theta \sin(\varphi + i\pi/2) \, \mathrm{d}\theta \, \mathrm{d}\varphi$
z	z	$\sin\theta \cos^2\theta \, \mathrm{d}\theta \, \mathrm{d}\varphi$

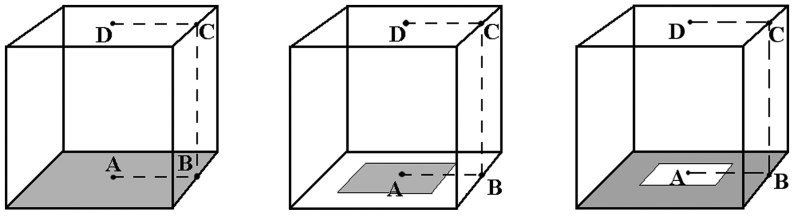

BMP-A *BMP-B* *BMP-C*

Fig. 4 BMP geometries, loads, and lines where solutions are given.

Equations (13) and (14) are similarly treated to yield

$$F_n(\mathbf{r}) = \sum_{k=1}^{6} \iiint_{V_k} e^{-\rho}\,\mathrm{d}\rho\,\mathrm{d}A_n = \sum_{i=1}^{4} \int_{\varphi=-\phi_i}^{\xi_i} \left\{ \int_{\theta=0}^{\theta_{ia}} (1-e^{-\rho_6})\,\mathrm{d}A_n + \int_{\theta=\theta_{ia}}^{\theta_{ib}} (1-e^{-\rho_i})\,\mathrm{d}A_n + \int_{\theta=\theta_{ib}}^{\pi} (1-e^{-\rho_5})\,\mathrm{d}A_n \right\} \tag{24}$$

and

$$F_{nm}(\mathbf{r}) = \sum_{k=1}^{6} \iiint_{V_k} e^{-\rho}\,\mathrm{d}\rho\,\mathrm{d}A_{nm} = \sum_{i=1}^{4} \int_{\varphi=-\phi_i}^{\xi_i} \left\{ \int_{\theta=0}^{\theta_{ia}} (1-e^{-\rho_6})\,\mathrm{d}A_{nm} + \int_{\theta=\theta_{ia}}^{\theta_{ib}} (1-e^{-\rho_i})\,\mathrm{d}A_{nm} + \int_{\theta=\theta_{ib}}^{\pi} (1-e^{-\rho_5})\,\mathrm{d}A_{nm} \right\} \tag{25}$$

The forcing functions [Eqs. (7–9)], which represent direct radiation from the source wall (or the patch), are also evaluated in the polar coordinate. The analytical expressions for these functions are given in [24], and these expressions can be used in this study as well, since they are independent of the anisotropy of the medium.

IV. Results and Discussion

Three benchmark problems (BMPs) were adopted in this study. The cubic enclosures ($x_0 = y_0 = z_0 = 1$ optical thickness) and the external source locations (uniform and nonuniform loads) considered in the study are given in Fig. 4. These BMPs are described as follows:

1) Benchmark problem A (BMP-A) is a uniform diffuse source of unit strength ($I_D = 1$) distributed over the bottom wall.

2) Benchmark problem B (BMP-B) is a uniform diffuse source of unit strength distributed over a square patch bounded by $-x_0/2 \le x \le x_0/2$ and $-y_0/2 \le y \le y_0/2$ at the bottom wall.

3) Benchmark problem C (BMP-C) is a uniform diffuse source of unit strength distributed over the square-annular region at the bottom wall. The inner square without the source is bounded by $-x_0/2 \le x \le x_0/2$ and $-y_0/2 \le y \le y_0/2$.

A. Grid Sensitivity and Validity of Results

In Tables 2 and 3, a grid sensitivity analysis for $\omega_0 = 1$ and $\bar{a} = 1$ of the BMP-B case is given. The incident energy and the net radiative heat flux solutions obtained using the DOM S_8 and the RITEs are tabulated for selected nodes along the diagonal line connecting $(0, 0, 0)$ to (x_0, y_0, z_0). The DOM and the RITE solutions are obtained using a $65 \times 65 \times 65$ grid, but the RITEs solutions for the $17 \times 17 \times 17$ and $33 \times 33 \times 33$ grid cases are presented in percent relative error with respect to those of the $65 \times 65 \times 65$ grid, computed as follows:

$$\text{Relative Error}\,(\%) = \frac{\text{Value}_{n\times n\times n} - \text{Value}_{65\times 65\times 65}}{\text{Value}_{65\times 65\times 65}} \times 100, \qquad n = 17 \quad \text{or} \quad 33 \tag{26}$$

The DOM S_8 solutions are obtained to validate our RITE code solutions. The DOM and the RITE solutions confirm the validity of our code solutions. Using the RITE solutions, the maximum relative errors for the incident energy are 0.425 and 0.036% for the $17 \times 17 \times 17$ and $33 \times 33 \times 33$ grid configurations, respectively. The maximum relative errors for the net heat fluxes, q_x or q_y, are 0.634% for the $17 \times 17 \times 17$ grid and 0.076% for the $33 \times 33 \times 33$ grid. On the other hand, the maximum errors in the net heat flux q_z are 0.47 and 0.08% for the $17 \times 17 \times 17$ and $33 \times 33 \times 33$ grid cases, respectively. Among the equally spaced integration quadrature methods, Boole's rule has a sixth-order approximation error, as mentioned earlier; therefore, it is possible to attain higher accuracy with fewer grid points in comparison with methods such as Simpson's rule, which has a fourth-order approximation error. As an indication of the average deviation from $65 \times 65 \times 65$ grid solutions, the average relative errors of the tabulated data were computed from

$$\sum_{i=1}^{9} |\text{Relative Error}_i|/9$$

and also listed in Tables 2 and 3 for the $17 \times 17 \times 17$ and $33 \times 33 \times 33$ grid cases. It should be noted that the average of the relative error of the $17 \times 17 \times 17$ grid solution is about 10 times that of the $33 \times 33 \times 33$ grid. From the linear extrapolation from the $33 \times 33 \times 33$ grid, the tabulated $65 \times 65 \times 65$ grid data yield, in magnitude, relative errors of about 0.002% or less; thus, we estimate that the results for the $65 \times 65 \times 65$ grid are at least four or five significant-figure accurate.

B. Symmetry, Superposition Issues, and Computational Time

The symmetry feature of the BMPs was also incorporated into the numerical solution algorithm. The BMPs considered in this study are

Table 2 Grid sensitivity analysis for $\omega_0 = 1$ and $\bar{a} = 1$ of BMP-B

Location		DOM S_8			Present Solution $65 \times 65 \times 65$ grid		
$x = y$	z	G	$4q_x$	$4q_z$	G	$4q_x$	$4q_z$
0	0	0.53717	0.00110	0.95248	0.53519	0.00000	0.94320
0.0625	0.125	0.30358	0.01537	0.76966	0.29343	0.07016	0.73489
0.1250	0.250	0.15694	0.13788	0.41426	0.14192	0.10198	0.39255
0.1875	0.375	0.06180	0.07220	0.15238	0.07299	0.07541	0.19677
0.2500	0.500	0.04598	0.05929	0.11552	0.04205	0.05031	0.10884
0.3125	0.625	0.03348	0.04129	0.08984	0.02610	0.03418	0.06596
0.3750	0.750	0.02873	0.03762	0.08143	0.01675	0.02382	0.04232
0.4375	0.875	0.01946	0.02737	0.05623	0.01069	0.01661	0.02794
0.5000	1.000	0.00742	0.01260	0.02145	0.00630	0.01072	0.01829

Table 3 Changes in relative errors with refined grids

Location		Relative Error, %					
		$17 \times 17 \times 17$ grid			$33 \times 33 \times 33$ grid		
$x = y$	z	G	$4q_x$	$4q_z$	G	$4q_x$	$4q_z$
0	0	0.102	0.000	−0.076	0.024	0.000	−0.024
0.0625	0.125	0.425	−0.634	0.466	−0.006	−0.076	−0.081
0.1250	0.250	−0.021	−0.208	−0.316	0.020	−0.042	−0.021
0.1875	0.375	0.411	−0.554	0.377	0.012	−0.016	−0.032
0.2500	0.500	0.159	−0.042	0.059	0.033	−0.010	0.015
0.3125	0.625	0.375	−0.231	0.444	0.027	0.006	0.002
0.3750	0.750	0.137	0.055	0.033	0.036	0.004	0.024
0.4375	0.875	0.225	−0.235	0.344	0.028	0.012	0.004
0.5000	1.000	0.095	0.065	0.131	0.016	0.009	0.027
Average error		0.217	0.225	0.250	0.022	0.019	0.026

Table 4 Incident energy and net partial heat flux q_z solutions of BMP-A, BMP-B, and BMP-C at points C and D for $\bar{a} = -1.0$, $\bar{a} = 1.0$, and $\omega_0 = 0.5$ cases

	$\bar{a} = -1.0$		$\bar{a} = 1.0$	
	G	$4q_z$	G	$4q_z$
		BMP-A		
Point C	0.01872	0.06392	0.02259	0.07534
Point D	0.02640	0.09311	0.03228	0.11218
		BMP-B		
Point C	0.00525	0.01797	0.00641	0.02142
Point D	0.00823	0.03022	0.01001	0.03625
		BMP-C		
Point C	0.01347	0.04595	0.01618	0.05392
Point D	0.01817	0.06289	0.02227	0.07593

symmetrical with respect to the $x = 0$ and $y = 0$ planes; thus, we observe

$$G(x, y, z) = G(x, -y, z) = G(-x, y, z) = G(-x, -y, z)$$

for the incident energy. Symmetry relations can be similarly constructed for the net radiative heat flux components as well. Thus, by copying the incident energy and the heat flux solutions to other regions, the computation time is reduced by $\frac{3}{4}$. It should also be noted that the superposition technique, which was described in [24], could also used in the present study. For example, in Table 4, the incident energy G and the net partial heat flux q_z solutions at points C and D are tabulated for $\bar{a} = \pm 1.0$ and $\omega_0 = 0.5$ of BMP-A, BMP-B, and BMP-C. It is observed that the pertinent solutions for BMP-C could

Table 5 Incident energy and net partial heat fluxes of BMP-A along AB, BC and CD lines for $\bar{a} = -1.0$, $\bar{a} = 1.0$, and $\omega_0 = 0.01$

Path	$\bar{a} = -1.0$			$\bar{a} = 1.0$		
	G	$4q_y$	$4q_z$	G	$4q_y$	$4q_z$
AB, y/y_0						
0.000	0.50094	0.00000	0.99815	0.50048	0.00000	0.99930
0.125	0.50093	0.00008	0.99816	0.50048	0.00006	0.99930
0.250	0.50092	0.00017	0.99818	0.50047	0.00012	0.99931
0.375	0.50090	0.00026	0.99822	0.50046	0.00018	0.99933
0.500	0.50087	0.00036	0.99829	0.50044	0.00025	0.99935
0.625	0.50082	0.00048	0.99838	0.50042	0.00033	0.99938
0.750	0.50075	0.00062	0.99853	0.50039	0.00042	0.99943
0.875	0.50064	0.00079	0.99876	0.50035	0.00052	0.99950
1.000	0.25041	0.50095	0.49928	0.25025	0.50063	0.49966
BC, z/z_0						
0.125	0.15969	0.29919	0.39257	0.15970	0.29924	0.39304
0.250	0.11092	0.19868	0.30478	0.11099	0.19885	0.30528
0.375	0.07834	0.13416	0.23275	0.07843	0.13436	0.23324
0.500	0.05601	0.09142	0.17613	0.05610	0.09162	0.17657
0.625	0.04053	0.06284	0.13298	0.04061	0.06301	0.13336
0.750	0.02967	0.04357	0.10059	0.02975	0.04372	0.10091
0.875	0.02196	0.03049	0.07641	0.02203	0.03062	0.07667
1.000	0.01641	0.02151	0.05836	0.01648	0.02163	0.05856
CD, y/y_0						
0.875	0.01757	0.02017	0.06328	0.01765	0.02028	0.06352
0.750	0.01865	0.01834	0.06787	0.01873	0.01844	0.06814
0.625	0.01962	0.01606	0.07201	0.01971	0.01614	0.07230
0.500	0.02045	0.01337	0.07558	0.02054	0.01344	0.07589
0.375	0.02112	0.01034	0.07846	0.02121	0.01039	0.07878
0.250	0.02161	0.00705	0.08058	0.02171	0.00708	0.08091
0.125	0.02191	0.00357	0.08188	0.02201	0.00359	0.08221
0.000	0.02201	0.00000	0.08231	0.02211	0.00000	0.08265

Table 6 Incident energy and net partial heat fluxes of BMP-A along AB, BC, and CD lines for $\bar{a} = -1.0$, $\bar{a} = 1.0$, and $\omega_0 = 0.5$

		$\bar{a} = -1.0$			$\bar{a} = 1.0$	
Path	G	$4q_y$	$4q_z$	G	$4q_y$	$4q_z$
AB, y/y_0						
0.000	0.55234	0.00000	0.89685	0.52724	0.00000	0.95800
0.125	0.55211	0.00477	0.89730	0.52713	0.00350	0.95818
0.250	0.55139	0.00972	0.89870	0.52679	0.00709	0.95872
0.375	0.55013	0.01502	0.90118	0.52619	0.01086	0.95966
0.500	0.54821	0.02087	0.90502	0.52530	0.01490	0.96108
0.625	0.54541	0.02750	0.91069	0.52404	0.01932	0.96311
0.750	0.54135	0.03513	0.91908	0.52226	0.02426	0.96599
0.875	0.53519	0.04400	0.93218	0.51964	0.02989	0.97033
1.000	0.27263	0.55269	0.46029	0.26440	0.53606	0.47953
BC, z/z_0						
0.125	0.18176	0.35176	0.37788	0.18199	0.35409	0.40129
0.250	0.12902	0.24152	0.30104	0.13249	0.25017	0.32627
0.375	0.09253	0.16737	0.23426	0.09728	0.17800	0.25881
0.500	0.06686	0.11651	0.18002	0.07195	0.12721	0.20245
0.625	0.04867	0.08140	0.13785	0.05363	0.09137	0.15751
0.750	0.03560	0.05693	0.10584	0.04027	0.06594	0.12254
0.875	0.02605	0.03954	0.08183	0.03037	0.04762	0.09571
1.000	0.01873	0.02645	0.06391	0.02259	0.03332	0.07534
CD, y/y_0						
0.875	0.02041	0.02471	0.07008	0.02494	0.03096	0.08387
0.750	0.02190	0.02239	0.07571	0.02683	0.02793	0.09102
0.625	0.02321	0.01953	0.08074	0.02844	0.02430	0.09724
0.500	0.02433	0.01621	0.08504	0.02980	0.02013	0.10247
0.375	0.02522	0.01251	0.08850	0.03087	0.01550	0.10666
0.250	0.02587	0.00851	0.09104	0.03165	0.01053	0.10970
0.125	0.02627	0.00431	0.09259	0.03212	0.00533	0.11156
0.000	0.02640	0.00000	0.09311	0.03228	0.00000	0.11218

be obtained from the solutions of BMP A − BMP B or, similarly, the solutions of BMP-A could be constructed from the BMP B + BMP C solutions, etc.

This study was carried out using an Intel E4600 at 2.40 GHz 2 GB RAM PC. The computational (CPU) time was about 11 s, 10.2 min., and 9.1 h for the $17 \times 17 \times 17$, $33 \times 33 \times 33$, and $65 \times 65 \times 65$ grid cases, respectively.

C. Results for Participating Medium

The incident energy and the net heat flux solutions for $\omega_0 = 0.01$ and $\bar{a} = \pm 1$ (backward and forward scattering) of BMP-A are tabulated for selected points along the lines AB, BC, and CD in Table 5. Since scattering is minimal (almost purely absorbing media), the tabulated RITE solutions are dominated by Eqs. (7–9). It is important to note that these functions are discontinuous at the edges

Table 7 Incident energy and net partial heat fluxes of BMP-A along AB, BC, and CD lines for $\bar{a} = -1.0$, $\bar{a} = 1.0$, and $\omega_0 = 1.0$

		$\bar{a} = -1.0$			$\bar{a} = 1.0$	
Path	G	$4q_y$	$4q_z$	G	$4q_y$	$4q_z$
AB, y/y_0						
0.000	0.62089	0.00000	0.76034	0.56418	0.00000	0.89512
0.125	0.62030	0.01165	0.76152	0.56390	0.00869	0.89559
0.250	0.61848	0.02365	0.76514	0.56306	0.01755	0.89704
0.375	0.61530	0.03638	0.77151	0.56159	0.02676	0.89954
0.500	0.61050	0.05020	0.78122	0.55942	0.03649	0.90327
0.625	0.60363	0.06553	0.79530	0.55637	0.04696	0.90853
0.750	0.59386	0.08275	0.81564	0.55212	0.05840	0.91589
0.875	0.57946	0.10216	0.84640	0.54598	0.07108	0.92671
1.000	0.30158	0.62044	0.40877	0.28408	0.58453	0.44866
BC, z/z_0						
0.125	0.21351	0.42791	0.35729	0.21272	0.42969	0.40437
0.250	0.15719	0.30878	0.29703	0.16332	0.32438	0.34752
0.375	0.11605	0.22297	0.23919	0.12543	0.24415	0.28868
0.500	0.08582	0.16075	0.18942	0.09653	0.18357	0.23528
0.625	0.06351	0.11554	0.14925	0.07453	0.13812	0.19020
0.750	0.04682	0.08230	0.11795	0.05765	0.10384	0.15359
0.875	0.03402	0.05719	0.09404	0.04439	0.07730	0.12459
1.000	0.02352	0.03657	0.07580	0.03280	0.05361	0.10216
CD, y/y_0						
0.875	0.02631	0.03423	0.08483	0.03726	0.04952	0.11693
0.750	0.02872	0.03099	0.09289	0.04059	0.04442	0.12843
0.625	0.03081	0.02699	0.10002	0.04335	0.03845	0.13814
0.500	0.03257	0.02237	0.10607	0.04562	0.03171	0.14618
0.375	0.03397	0.01723	0.11092	0.04740	0.02435	0.15252
0.250	0.03499	0.01171	0.11446	0.04868	0.01651	0.15710
0.125	0.03561	0.00592	0.11662	0.04945	0.00834	0.15988
0.000	0.03582	0.00000	0.11734	0.04971	0.00000	0.16081

and the corners of the diffuse source region. To save space, we will illustrate this feature only for f_G, which is explicitly given in [24] as

$$f_G(x,y,z)=\frac{I_D}{4\pi}\sum_{i=1}^{4}\int_{\varphi=-\phi_i}^{\xi_i}\left\{E_2(z)-\frac{z}{\sqrt{\rho_i^2+z^2}}E_2\left(\sqrt{\rho_i^2+z^2}\right)\right\}\mathrm{d}\varphi \tag{27}$$

where $E_2(z)$ is the second-order exponential integral function [25]. For the diffuse source region ($z=0$), we have $I_D=1$ and $E_2(0)=1$. In this case, Eq. (27) is reduced to

$$f_G(x,y,0)=\frac{1}{4\pi}\sum_{i=1}^{4}\int_{\varphi=-\phi_i}^{\xi_i}\mathrm{d}\varphi$$

which is clearly independent of the spatial variables; that is, f_G is constant throughout the source region. For an interior (x,y) point, the polar integration interval is over 2π (see Fig. 2), which yields

$$\sum_{i=1}^{4}\int_{\varphi=-\phi_i}^{\xi_i}\mathrm{d}\varphi=2\pi$$

and so one obtains $f_G(x,y,0)=0.5$. For the edge of the diffuse source, by moving the interior node to the edge, four of the eight triangular regions vanish to give

$$\sum_{i=1}^{4}\int_{\varphi=-\phi_i}^{\xi_i}\mathrm{d}\varphi=\pi$$

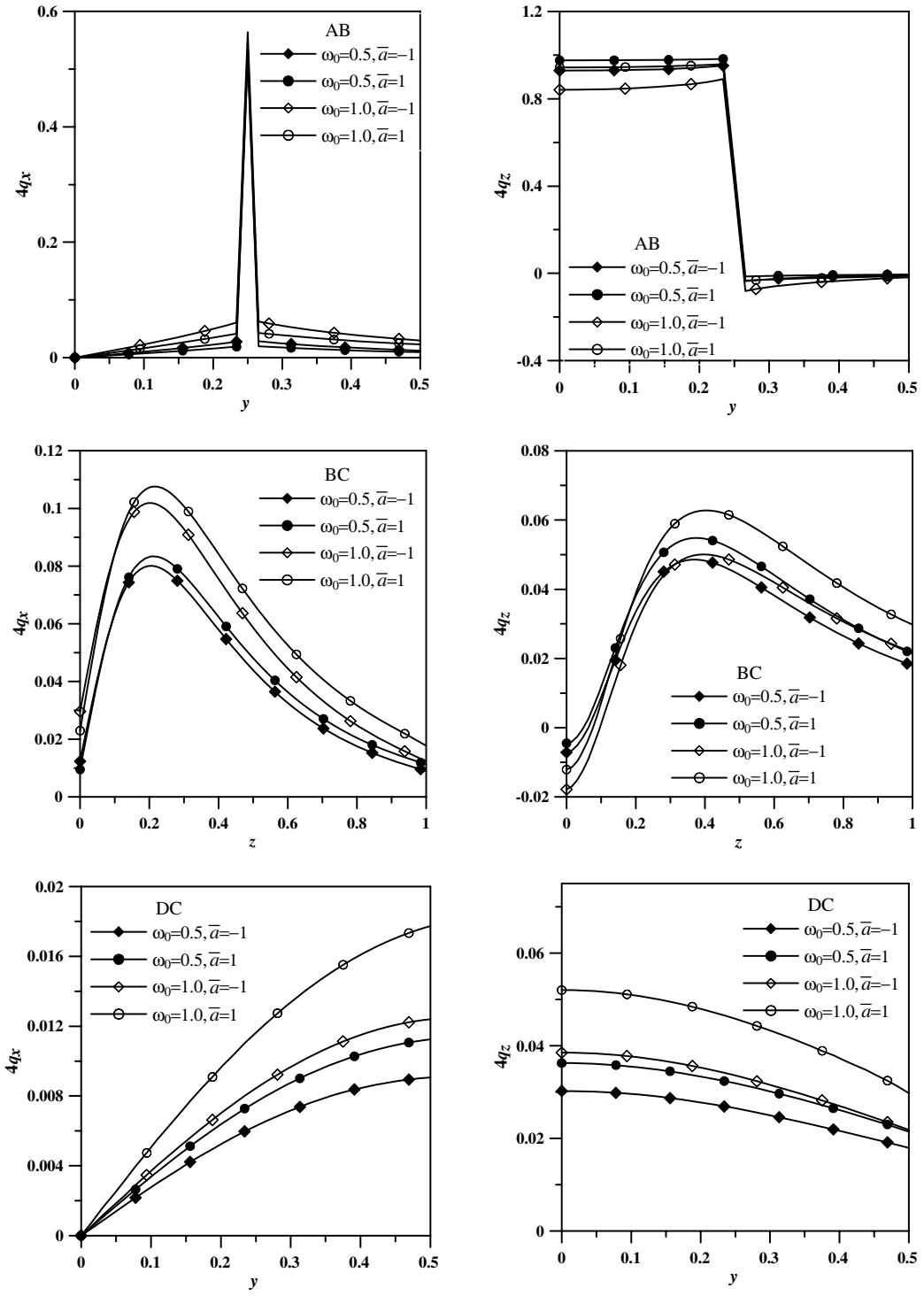

Fig. 5 Net partial heat fluxes of BMP-B along AB, BC, and DC lines for $\bar{a}=-1.0$, $\bar{a}=1.0$, $\omega_0=0.5$, and $\omega_0=1.0$.

which yields $f_G(x, y, 0) = 0.25$. On the other hand, for the corners of the source region, this time we obtain

$$\sum_{i=1}^{4} \int_{\varphi=-\phi_i}^{\xi_i} \mathrm{d}\varphi = \frac{\pi}{2}$$

and thus $f_G(x, y, 0) = 0.125$. For this reason, the incident radiation G and the net radiative heat flux components are almost constant from A to B due to the incidence of a constant diffuse source. However, a sharp drop in the incident energy or rise in the net radiative heat fluxes is observed due to the discontinuities experienced in the expressions for f_G, f_x, f_y, and f_z. For instance, in the purely absorbing case, G drops down to 0.25 from 0.5 while q_y rises to 0.5 from 0 and q_z drops down to 0.5 from 1. On the other hand, the incident radiation and the heat flux components are continuous on lines BC and CD (Table 5). These discontinuities are not encountered in the DOM since the physical quantities are computed for the centroids of the control volumes. The incident radiation and the heat flux components decrease along the line from B to C as the magnitude of the source function decreases. Because of the symmetry of the physical problem at point D, the incident energy is at a maximum while the net radiative heat fluxes are at a minimum. The solutions for both the backward and forward scattering cases are almost identical, since the effects of the anisotropy terms of the RITEs diminish as $\omega_0 \to 0$.

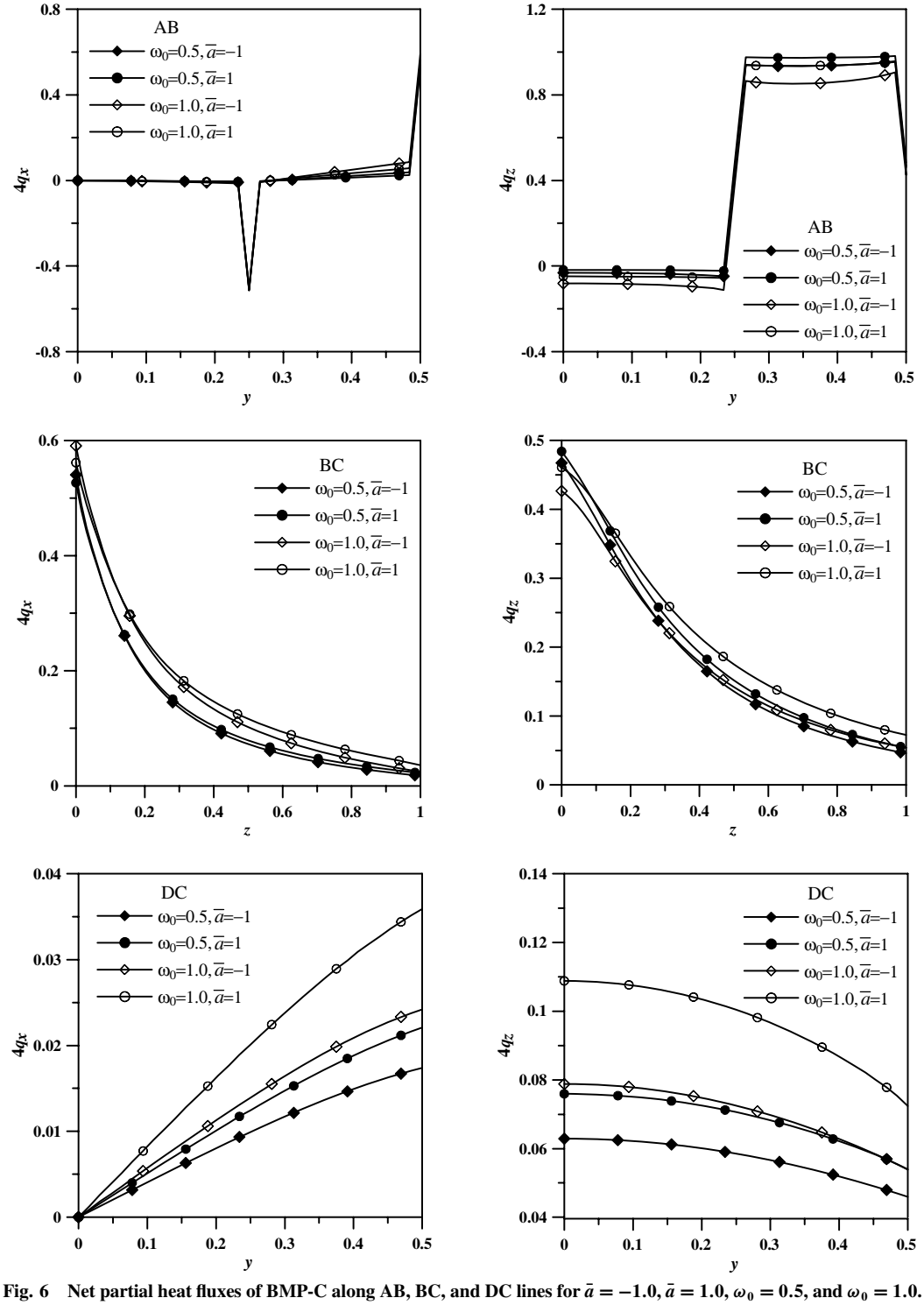

Fig. 6 Net partial heat fluxes of BMP-C along AB, BC, and DC lines for $\bar{a} = -1.0$, $\bar{a} = 1.0$, $\omega_0 = 0.5$, and $\omega_0 = 1.0$.

The incident energy and the net heat flux solutions for $\omega_0 = 0.5$ and $\bar{a} = \pm 1$ (backward and forward scattering) of BMP-A are tabulated for selected points along the lines AB, BC, and CD in Table 6. The incident radiation G slightly decreases from points A to B, while q_z increases as expected, since thermal radiation leaks out of the sidewall at B. A sharp drop in G and q_z is observed at point B, which is caused by the source discontinuity mentioned earlier. On the other hand, q_y is zero at A, since this point is located on the symmetry planes. For both scattering cases, q_y slightly increases when moving toward B, where it jumps slightly above 0.5 due to the discontinuity of f_x or f_y at the edge. The magnitudes of G and q_y are greater in the backward scattering case, while q_z is greater in the forward scattering case along line AB. The incident radiation and the net heat flux components decrease along line BC as the thermal radiation is absorbed by the medium. The numerical solutions (G and q_y) of the backward scattering case at the bottom wall are higher than those of forward scattering; but away from the diffuse source plane, the medium receives more of the scattered energy within the enclosure, thereby yielding an increase in the incident energy and the net radiative heat fluxes. The incident energy and the net radiative heat fluxes are greater for the forward scattering case than for the backward scattering case.

The incident energy and the net heat flux solutions for $\omega_0 = 1.0$ and $\bar{a} = \pm 1$ (backward and forward scattering) of BMP-A are tabulated for selected points along lines AB, BC, and CD in Table 7. Basically the solution profiles along the selected paths that were observed for the $\omega_0 = 0.5$ case are observed here as well. Along lines AB and BC, G and q_y increase, but q_z decreases with increasing scattering albedo. Along the CD line, G, q_y, and q_z increase with increasing scattering albedo. Higher numerical values are due to larger scattering of the medium.

Figure 5 depicts the net heat flux profiles (q_x and q_z) for $\omega_0 = 0.5$ and 1.0 and $\bar{a} = \pm 1$ (backward/forward scattering) of BMP-B along lines AB, BC, and CD. The net heat flux q_x starts at zero at the central point A and slightly increases to up to $x = 0.25$, where it jumps to 0.50 (at the diffuse source's edge discontinuity) and then steadily decreases toward point B. The magnitude of q_x is higher in the $\omega_0 = 1.0$ cases, while the flux profile of the backward scattering case is higher than that of the forward scattering case. Not only is the flux magnitude smaller in the $\omega_0 = 0.5$ case, but the difference between the profiles of forward and backward scattering is minimal. While q_z is constant up to $x = 0.25$ due to constant incident radiation, it drops to zero beyond $x = 0.25$ where there is no incident radiation in this range. In fact, in the backward scattering case for $\omega_0 = 1$, some thermal radiation leakage from the bottom surface is observed for $x > 0.25$. As the scattering albedo increases, along the BC line, q_x also increases due to increased scattering within the medium. In both scattering albedo cases, as expected, the forward scattering solutions are slightly higher than those of backward scattering. The net radiative heat flux solutions of the $\omega_0 = 1.0$ case for both q_x and q_z are greater than those of the $\omega_0 = 0.5$ case due to increased scattering taking place within the medium. However, at point B, radiative energy leakage increases with increased scattering for both backward and forward scattering. Along the DC line, q_x increases from zero at point D (on the symmetry plane) while moving toward point C due to radiative energy streaming out horizontally from the sidewalls. The streaming energy increases with scattering albedo and forward scattering. On the other hand, q_z decreases from its maximum value at point D while moving toward C and, for the same reasons, the radiation leakage increases with scattering albedo and forward scattering.

The net heat flux solutions (q_x and q_z) for $\omega_0 = 0.5$ and 1.0 and $\bar{a} = \pm 1$ (backward/forward scattering) of BMP-C along lines AB, BC, and CD are depicted in Fig. 6. From points A to B along the AB line, q_x is zero since there is no incident energy in this interval, but q_x drops to -0.5 at the discontinuity ($x = 0.25$); it then increases while moving toward point A where the radiative energy streams out. The flux profiles are almost identical. However, the q_x profiles for the $\omega_0 = 1.0$ cases are slightly higher than those of the $\omega_0 = 0.5$ case while moving toward the discontinuity at point B where q_x jumps to a value of 0.5. Similarly, q_z in the $0 < x < 0.25$ interval is negative, which implies that the radiative energy is leaking from the inner square patch that has no incident radiation. The amount of leakage increases with the scattering albedo and backward scattering. At the point of discontinuous incident energy ($x = 0.25$), q_z jumps to a constant value of one for an absorbing medium and decreases with increasing scattering albedo and backward scattering. At point B, which is on the edge of the diffuse wall, the net heat flux q_z drops sharply to 0.5 due to the discontinuity. Along the BC line, the net radiative heat fluxes q_x and q_z decrease while moving toward point C as the distance from the bottom plane (or the diffuse source) increases. The flux profiles depict an increase with increasing scattering albedo and forward scattering. While moving toward point C with increasing scattering albedo and forward scattering, q_x increases from zero at point D. On the other hand, q_z decreases from its maximum value at point D while moving toward point C. As mentioned before, radiation leakage increases with scattering albedo and forward scattering.

V. Conclusions

Three-dimensional RITEs for a cubic ($x_0 = y_0 = z_0 = 1$ optical thickness) absorbing, emitting, and anisotropically scattering homogeneous medium are numerically solved using the subtraction of singularity technique. To remove the singularities of the integral kernels and boundary source terms of the RITEs, coordinate transformations followed by analytical treatment are introduced to ensure highly accurate solutions. The resulting system of linear equations from the RITEs is solved iteratively. Three BMPs for a cold participating medium, subjected to externally diffuse radiation loads in various combinations, are considered, and the solutions for the incident energy and the net radiative heat flux components are given in tabular and/or graphical form for scattering albedos of $\omega_0 = 0.01$, 0.5, and 1.

References

[1] Beach, H. L., Özışık, M. N., and Siewert, C. E., "Radiative Transfer in Linearly Anisotropic Scattering, Conservative and Nonconservative Slabs with Reflective Boundaries," *International Journal of Heat and Mass Transfer*, Vol. 14, No. 10, 1971, pp. 1551–1565. doi:10.1016/0017-9310(71)90066-4

[2] Dayan, A., and Tien, C. L., "Heat Transfer in a Gray Planar Medium with Linear Anisotropic Scattering," *Journal of Heat Transfer*, Vol. 97, No. 3, 1975, pp. 391–396. doi:10.1115/1.3450385

[3] Boffi, V. C., and Spiga, G., "Integral Theory of Radiative Heat Transfer with Anisotropic Scattering and General Boundary Conditions," *Journal of Mathematical Physics*, Vol. 18, No. 12, 1977, pp. 2448–2455. doi:10.1063/1.523207

[4] Modest, M. R., and Azad, F. H., "The Influence and Treatment of Mie Scattering in Radiative Heat Transfer," *Journal of Heat Transfer*, Vol. 102, No. 1, 1980, pp. 92–98. doi:10.1115/1.3244255

[5] Azad, F. H., and Modest, M. R., "Evaluation of the Radiative Heat Flux in Absorbing, Emitting and Linear Anisotropically Scattering Cylindrical Media," *Journal of Heat Transfer*, Vol. 103, No. 2, 1981, pp. 350–356. doi:10.1115/1.3244465

[6] Stephens, G. L., "Radiative Transfer in Spatially Heterogeneous Two Dimensional, Anisotropically Scattering Media," *Journal of Quantitative Spectroscopy and Radiative Transfer*, Vol. 36, No. 1, 1986, pp. 51–67. doi:10.1016/0022-4073(86)90015-4

[7] Kim, T. K., and Lee, H., "Effect Of Anisotropic Scattering on Radiative Heat Transfer in Two Dimensional Rectangular Enclosures," *International Journal of Heat and Mass Transfer*, Vol. 31, No. 8, 1988, pp. 1711–1721. doi:10.1016/0017-9310(88)90283-9

[8] Tan, Z., "Radiative Heat Transfer in Multidimensional Emitting, Absorbing, and Anisotropic Scattering Media-Mathematical Formulation and Numerical Method," *Journal of Heat Transfer*, Vol. 111, No. 1, 1989, pp. 141–147. doi:10.1115/1.3250636

[9] Thynell, S. T., "The Integral Form of the Equation of Transfer in Finite, Two-Dimensional, Cylindrical Media," *Journal of Quantitative Spectroscopy and Radiative Transfer*, Vol. 42, No. 2, 1989, pp. 117–136. doi:10.1016/0022-4073(89)90094-0

[10] Crosbie, A. L., and Dougherty, R. L., "Two-Dimensional Radiative Transfer in a Cylindrical Geometry with Anisotropic Scattering," *Journal of Quantitative Spectroscopy and Radiative Transfer*, Vol. 25, No. 6, 1981, pp. 551–569. doi:10.1016/0022-4073(81)90030-3

[11] Altaç, Z., "Radiative Transfer in Absorbing, Emitting and Linearly Anisotropic-Scattering Inhomogeneous Cylindrical Medium," *Journal of Quantitative Spectroscopy and Radiative Transfer*, Vol. 77, No. 2, 2003, pp. 177–192. doi:10.1016/S0022-4073(02)00086-9

[12] Altaç, Z., and Tekkalmaz, M., "Solution of the Radiative Integral Transfer Equations in Rectangular Absorbing, Emitting, and Anisotropically Scattering Homogeneous Medium," *Journal of Heat Transfer*, Vol. 126, No. 1, 2004, pp. 137–139. doi:10.1115/1.1578503

[13] Crosbie, A. L., and Lee, L. C., "Relation Between Multidimensional Radiative Transfer in Cylindrical and Rectangular Coordinates with Anisotropic Scattering," *Journal of Quantitative Spectroscopy and Radiative Transfer*, Vol. 38, No. 3, 1987, pp. 231–241. doi:10.1016/0022-4073(87)90091-4

[14] Mengüç, M. P., and Viskanta, R., "Radiative Transfer in Three-Dimensional Rectangular Enclosures Containing Inhomogeneous, Anisotropically Scattering Media," *Journal of Quantitative Spectroscopy and Radiative Transfer*, Vol. 33, No. 6, 1985, pp. 533–549. doi:10.1016/0022-4073(85)90021-4

[15] An, W., Ruan, L. M., Qi, H., and Liu, L. H., "Finite Element Method for Radiative Heat Transfer in Absorbing and Anisotropic Scattering Media," *Journal of Quantitative Spectroscopy and Radiative Transfer*, Vol. 96, Nos. 3–4, 2005, pp. 409–422. doi:10.1016/j.jqsrt.2004.12.010

[16] Boulet, P., Collin, A., and Consalvi, J. L., "On the Finite Volume Method and Discrete Ordinates Method Regarding Radiative Heat Transfer in Acute Forward Anisotropic Scattering Media," *Journal of Quantitative Spectroscopy and Radiative Transfer*, Vol. 104, No. 3, 2007, pp. 460–473. doi:10.1016/j.jqsrt.2006.09.010

[17] Jiang, Y. Y., "A Two Step Strategy for Numerical Simulation of Radiative Transfer with Anisotropic Scattering And Reflection," *Journal of Quantitative Spectroscopy and Radiative Transfer*, Vol. 109, No. 4, 2008, pp. 636–649. doi:10.1016/j.jqsrt.2007.08.008

[18] Mueller, D. W., Jr., and Crosbie, A. L., "Three-Dimensional Radiative Transfer in an Anisotropically Scattering, Semi-Infinite Medium: Generalized Reflection Function," *Journal of Quantitative Spectroscopy and Radiative Transfer*, Vol. 74, No. 1, 2002, pp. 43–68. doi:10.1016/S0022-4073(01)00191-1

[19] Grissa, H., Askri, F., Ben Salah, M., and Ben Nasrallah, S., "Three-Dimensional Radiative Transfer Modeling Using the Control Volume Finite Element Method," *Journal of Quantitative Spectroscopy and Radiative Transfer*, Vol. 105, No. 3, 2007, pp. 388–404. doi:10.1016/j.jqsrt.2006.12.008

[20] Nunes, E. M., Modi, V., and Naraghi, M. H. N., "Radiative Transfer in Arbitrarily-Shaped Axisymmetric Enclosures with Anisotropic Scattering Media," *International Journal of Heat and Mass Transfer*, Vol. 43, No. 18, 2000, pp. 3275–3285. doi:10.1016/S0017-9310(99)00384-1

[21] Zhang, J. M., and Sutton, W. H., "Multidimensional Radiative Transfer in Absorbing, Emitting, and Linearly Anisotropic Scattering Cylindrical Medium with Space-Dependent Properties," *Journal of Quantitative Spectroscopy and Radiative Transfer*, Vol. 52, No. 6, 1994, pp. 791–808. doi:10.1016/0022-4073(94)90044-2

[22] Trivic, D. N., and Amon, C. H., "Modeling the 3-D Radiation of Anisotropically Scattering Media by Two Different Numerical Methods," *International Journal of Heat and Mass Transfer*, Vol. 51, Nos. 11–12, 2008, pp. 2711–2732. doi:10.1016/j.ijheatmasstransfer.2007.10.015

[23] Kim, S. H., and Huh, K. Y., "A New Angular Discretization Scheme of the Finite Volume Method for 3-D Radiative Heat Transfer in Absorbing, Emitting and Anisotropically Scattering Media," *International Journal of Heat and Mass Transfer*, Vol. 43, No. 7, 2000, pp. 1233–1242. doi:10.1016/S0017-9310(99)00211-2

[24] Altaç, Z., and Tekkalmaz, M., "Benchmark Solutions of Radiative Transfer Equation for Three-Dimensional Rectangular Homogeneous Media," *Journal of Quantitative Spectroscopy and Radiative Transfer*, Vol. 109, No. 4, 2008, pp. 587–607. doi:10.1016/j.jqsrt.2007.07.016

[25] Abramowitz, M., and Stegun, I. A., *Handbook of Mathematical Functions*, Dover, New York, 1972.